# Understanding of the fatigue crack nucleation in metallic sealing rings by explicitly incorporating the deformation history from manufacturing to service

Zebang Zheng [a,b,c,‡], Pandi Zhao [a,b,‡], Mei Zhan [b,⎺], Hongwei Li [b], Yudong Lei [b], M.W. Fu [c,*]

a. Research & Development Institute of Northwestern Polytechnical University in Shenzhen, Shenzhen, 518057, China

b. State Key Laboratory of Solidification Processing, Shaanxi Key Laboratory of High-Performance Precision Forming Technology and Equipment, School of Materials Science and Engineering, Northwestern Polytechnical University, Xi'an 710072, China

c. Department of Mechanical Engineering, Research Institute for Advanced Manufacturing, The Hong Kong Polytechnic University, Hung Hom, Kowloon, Hong Kong 999077, China

## Abstract

Fatigue cracking in metallic sealing rings has been a concern for the aerospace industry because the formation of even a micro-crack may cause an aviation accident. In this study, an integrated three-point bending fatigue experiment and dislocation-based crystal plasticity finite element modeling was used to determine the threshold for fatigue crack nucleation. Subsequently, the fatigue lives of the rings under different service conditions were evaluated based on the local stored energy density evolution. The conclusions of this work can provide theoretical guidance for the manufacturing of high-performance metallic sealing rings.

**Keywords:** fatigue crack nucleation, three-point bending, stored energy density, crystal plasticity, complex deformation history

‡ *These authors contributed equally to this work.*

⎺ *Corresponding author:* zhanmei@nwpu.edu.cn (M.Zhan)

* *Corresponding author:* ming.wang.fu@polyu.edu.hk (M.W. Fu)

# 1. Introduction

Metallic sealing rings made from nickel-based superalloys are critical components of aerospace engines that prevent the leakage of high-pressure liquid or gas fuel. It is required that there is no loss of sealing when the rings are subjected to the relative vibratory motion of adjacent pipes during the operation of engines. Otherwise, even a small amount of leakage could cause damage to the engine and provoke serious aviation accidents. The service life of such key components is highly related to the microstructure and operational environment [1–3]. The leakage of metallic rings mainly arises from two different reasons, compression-resilience reduction due to plastic deformations and microcrack formations under fatigue loadings. The former mainly results from the plastic strain accumulation during the service, the mechanism of which is relatively simple and capable of predicting. While for the latter, the life to crack in superalloys is difficult to quantify, and there is no apparent early sign of crack nucleations. Therefore, much effort has been directed toward the prediction and targeted prevention of microcrack formations during the service.

However, accurately capturing the deformation behavior of metallic sealing rings is challenging due to the complexity from both geometrical and mechanism aspects. On the one hand, the dimensions of the cross-sectional characteristics and the diameters of the rings are different by orders of magnitude. Taking W-shaped rings as an example, as shown in Fig. 1, the W-shaped section profile is formed within 6mm and the wall thickness is extremely thin (0.2~0.4mm), but the diameter of the ring can reach ~300mm [4]. The multi-pass rolling forming method, as in Fig. 1(b), for example, is generally applied to form such components [5]. The plastic responses of such components should be comprehensively considered over a wide range of lengths. On the other hand, the microcrack nucleation in nickel-based superalloys is affected by the microstructure and the deformation history from manufacturing to service. The service life optimization relies on the accurate prediction of microcrack nucleations, which depends on the microstructural features and stress histories in local regions [6–10].

Metallic sealing rings are generally manufactured by hydroforming and multi-pass rolling forming using thin-walled circular blanks. In 1965, Taylor [11] invented the forming method of an E-shaped sealing ring with long fatigue life. The forming of thin-walled components using high-strength alloys has been widely investigated to control ductile fracture and improve formability [12–17]. The cross-section profile of the rings has been developed into more complex geometries, including W-shaped [18], $\Omega$-shaped [19], C-shaped [20], O-shaped [21,22], and wave-shaped [23], etc., in recent years to improve the sealing performance and service stability. Shao et al. [19] have developed an external-internal composite spinning process to form thin-walled $\Omega$-shaped superalloy rings. They found that the forming defects such as wrinkling can be significantly reduced by using this trajectory compared with the conventional circular-straight roller one. Although advanced forming methods have been introduced recently, the work is more focused on overcoming the forming defects and improving the forming quality with respect to the geometrical requirements rather than their service performances.

As for the service stage, Wang et al. [24] introduced an analytical model to assess the reliability of the sealing performance of C-shaped rings in operational conditions. Hu et al. [25] proposed a two-dimensional axisymmetric model to analyze the failure of a V-shaped sealing ring and have found that the local stress concentration and the life of the sealing ring are greatly influenced by the magnitude of the sealing interference. Ding and Chen [26] utilized the finite element method to calculate the stress distribution of a three corrugated sealing ring and analyzed the effect of different corrugated radii on the mechanical properties of the rings in order to propose a preliminary design criterion. The work by Jia et al. [20] suggested that the finite element model can capture the compression-resilience

and linear load of C-shaped sealing rings with different diameters. Their results also indicated that internal pressure has an influence on the mechanical responses of the rings. Zhang and Hu [27] investigated the mechanical behavior and the sealing performance of O-shaped rings using the finite element method. The mechanical responses were found to be dependent on the compression ratio and the pressure of the sealing medium. Shen and co-authors [21] conducted a systematical investigation on the deformation characteristics and sealing performance of O-shaped rings using a nonlinear elastic-plastic finite element model. The investigations mentioned above focus on the responses of metallic rings during operations that were isolated from the manufacturing. Most of the analyses are based on the assumptions that the initial state of the rings before service is stress- and strain-free. Some models were also calibrated using raw materials which were assumed to have similar properties as the formed component. However, the metallic rings that will go into service have already experienced non-uniform and severe plastic deformation during the forming stage. Plastic inhomogeneity has been established at the microstructural level. As a result, there are residual stresses and strain distributed inhomogeneously within the rings before service. That initial state depends on the forming procedure and can significantly influence the lifetime of service. Thus, it is important to also consider the deformation history in order to assess the reliability of metallic rings accurately. Additionally, since there is no threshold being quantified for the microcrack formation in superalloys, the service life assessment of metallic rings is limited at the empirical level.
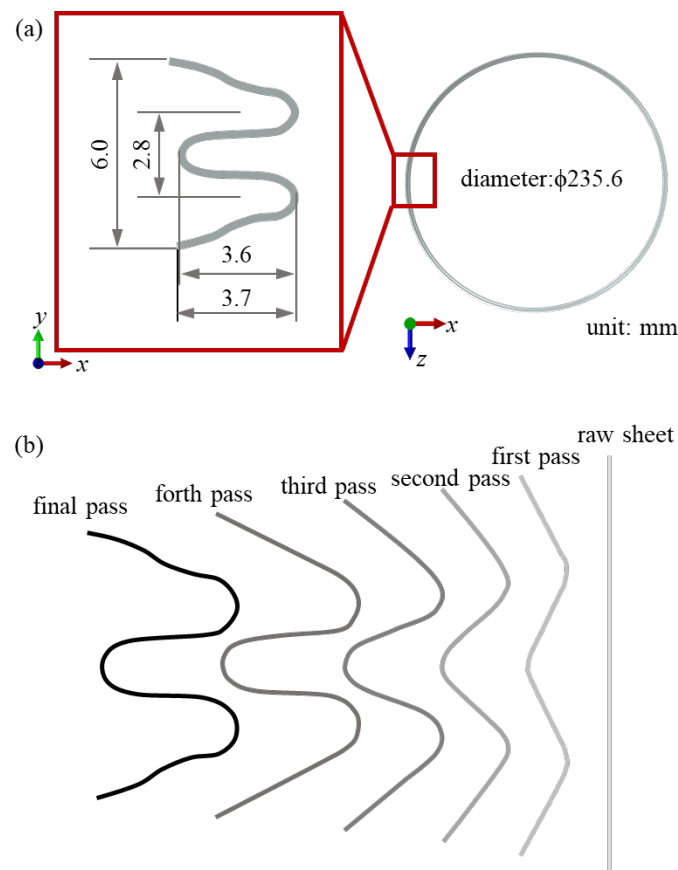


Fig. 1. The geometry of W-shaped metallic sealing rings [5]. (a) Dimensions of the cross-section and the ring; (b) schematic illustration of the multi-pass rolling forming track.

Therefore, in the present study, we take W-shaped metallic rings made from GH4169 nickel-based superalloys as the research object and consider the worst scenario where the rings were directly put into service after rolled forming without the annealing heat treatment. Although a specific problem is

discussed here, the investigation strategy can be generalized to predict the lifetime of other metallic sealing rings. The objective of the work consists of the following two aspects:

- Quantify the threshold for microcrack nucleation in the GH4169 superalloy.

- Evaluate the fatigue performance of metallic rings under different operational environments by considering the deformation history from manufacturing to service.

In order to achieve that goal, a systematic study integrating multiscale experiments and multiscale modeling techniques was established. The combination of quasi-in-situ three-point bending fatigue experiment, corresponding macroscopic finite element (FE) modeling and crystal plasticity finite element (CPFE) modeling was used to determine the threshold for microcrack nucleation of the material. The CPFE model is dislocation-based and rate-dependent, while the morphology replicates the real microstructure, so the length effect, rate sensitivity and microstructural features can be captured. The deformation histories from multi-pass rolling forming to different fatigue conditions were considered in FE modeling, from which the variation of local stress was extracted and applied as boundary conditions in the CPFE model to evaluate the service lifetime.

The paper is organized as follows: Section 2 outlines the experimental and computational methodology, including microstructure characterization, macroscopic strain rate sensitivity measurement, quasi-in-situ three-point bending, finite element, and crystal plasticity finite element modeling. Section 3 presents the determination of the critical stored energy for microcrack nucleation under cyclic loading in GH4169 superalloys. The determined threshold will be applied to the subsequent life assessment of metallic rings. In Section 4, the influences of three key service parameters, namely the preload $u$, the pressure of the sealed medium $p$, and the fatigue frequency $f$, on the service life of W-shaped sealing rings are comparatively studied by considering the deformation history from manufacturing to service. Finally, conclusions drawn from this study are presented in Section 5.

## 2. Methodology

### 2.1 Experimental Methodology

The material used in this study was produced by Gaona Aero Material Co., Ltd. via a cold rolling route. The thickness of the sheet for mechanical testing is 3mm. This sheet was produced by the same company as the raw material to form the W-shaped metallic sealing rings, and they both have the same chemical contents (as given in Table 1) and microstructural features, including grain morphology and texture. Macroscopic tensile test samples and quasi-in-situ three-point bending samples were fabricated as schematically illustrated in Fig. 2. The gauge length of the tensile samples is 30mm and the dimensions for the three-point bending sample are 20mm×6mm×3mm.

**Table 1.** Chemical compositions of GH4169 alloy (*wt* %)

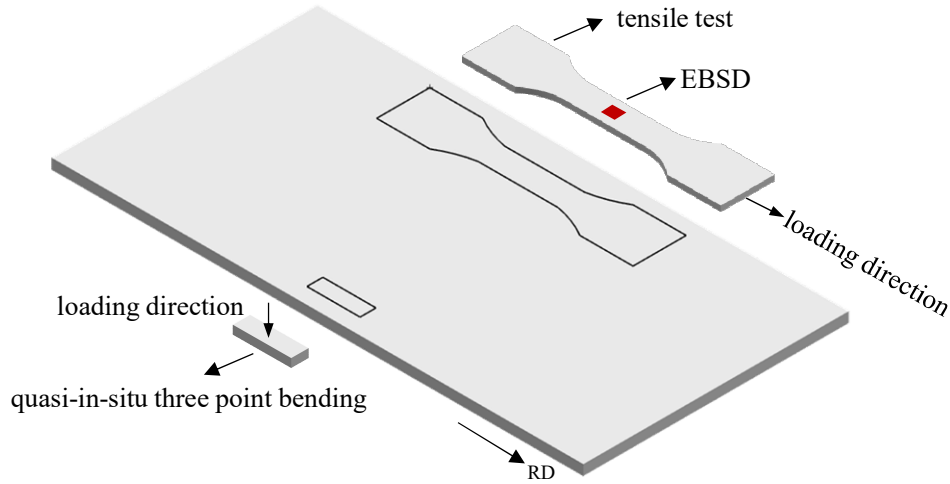| C | Si | Mn | S | P | Cr | Ni | Cu | Al | Ti | Nb | Co | Mo | Fe |
|---|----|----|----|----|----|----|----|----|----|----|----|----|----|
| 0.042 | 0.11 | 0.15 | 0.003 | 0.006 | 18.31 | 52.52 | 0.04 | 0.48 | 0.96 | 5.10 | 0.10 | 3.02 | Bal. |

**Fig. 2.** Schematic diagram of the sample fabrication.

● Microstructure characterization

Electron backscattered diffraction (EBSD) was conducted on the surface perpendicular to the normal direction (ND) within the gauge section of the tensile sample before deformation to characterize the initial microstructure of the material. The surface of the sample was polished using a series of grit silicon carbide papers followed by colloidal silica suspension treatment to remove the residual stresses that may have been introduced during the preparation. EBSD scanning was conducted on a field emission scanning electron microscope (SEM) from TESCAN equipped with a C-NANO EBSD detector from Oxford Instruments, using a step size of 0.3μm.

The three-point bending sample was prepared following the procedure and EBSD characterization was conducted at the bottom region of the surface perpendicular to the transerve direction (TD). A wide area of 1000μm × 300μm was scanned prior to deformation as the crack initiation site was unknown. SEM images of the same region were acquired during the interrupted three-point bending fatigue test until microcrack nucleation was observed. EBSD scanning around the crack was then conducted without further treatment on the surface to avoid the artificial effect. The location of the crack nucleation site thus can be identified together with the grain morphology and crystallographic orientations around.

● Strain rate sensitivity and three-point bending tests

The macroscopic mechanical properties of the material were measured by uniaxial tensile tests along RD under constant strain rates until failure. Three different strain rates range from $1 \times 10^{-5}\text{s}^{-1}$ to $1 \times 10^{-3}\text{s}^{-1}$ were considered. The strain during deformation was measured and recorded using a non-contact laser extensometer mounted on an Instron-8801 fatigue testing machine. From which the elastic modulus, yield strength and strain rate sensitivity (SRS) coefficient can be determined and the stress-strain curves can be used to calibrate the multiscale models.

Interrupted three-point bending fatigue testing was carried out on the pre-characterized rectangular sample. Cyclic loading with a maximum force $F_{app} = 2700N$, a force ratio of $R = 0$ and a frequency of 0.5Hz was applied to the punch. The residual displacement of the punch at the end of each loading cycle was recorded. Three repeated tests were preliminarily established until a visible crack appeared in the sample to estimate the life to microcrack nucleation. The number of cycles for visible crack was measured as ~9000. Another prepared sample was then interrupted loaded with SEM scanning every

1000 cycles for the first 7000 cycles, followed by every 500 cycles for the subsequent cycles. The accuracy of the life to crack nucleation can be limited to under 500 fatigue cycles.

## 2.2 Computational Methodology

● Finite element modeling

Two FE models were established in this study. The first one simulates the three-point fatigue experiment, as shown in Fig. 3(a). The geometries and relative locations of the sample, supporting rods and punch are identical to the experiment. The punch and supporting rods are designed as rigid bodies while the sample is deformable with the material properties implemented from the macroscopic tensile tests. The sample was meshed using C3D8R elements. Three elastic regions were defined near the contacting point between the sample and the punch and rods to avoid the burst of plastic deformation due to the singularity at the contact. The central region where large plastic deformation is expected was highly refined. The total number of elements is 43282 elements. The displacement of the punch at the end of each cycle under the applied loading condition can be well captured by the FE model without any additional fitting as shown in Fig. 3(b). The stress at the bottom center of the beam was extracted and applied as the boundary conditions in the CPFE model to determine the threshold for fatigue crack nucleation.
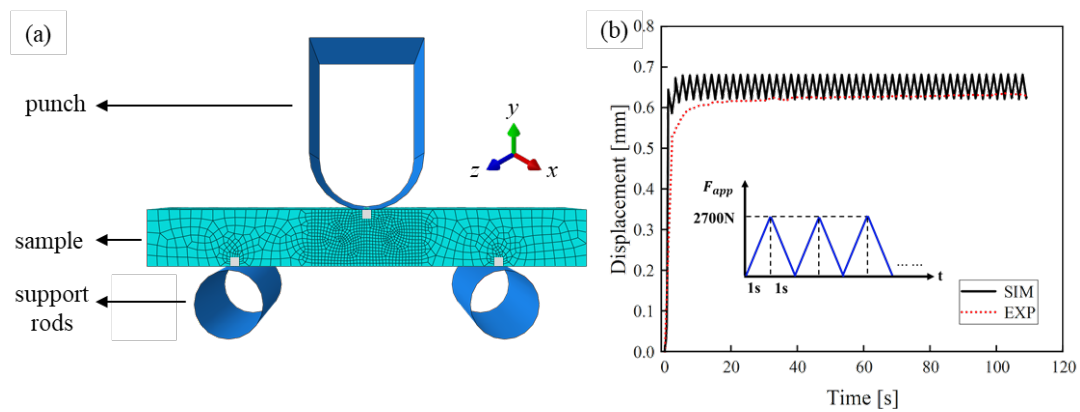


**Fig. 3.** The three-point bending FE model. (a) model setup; (b) comparison of the calculated displacement of the punch vs. the experimental recorded residual displacement at the end of each cycle.

The second FE model is used to simulate the multi-pass rolling forming and service process of metallic sealing rings. The blank is a circular strip with the size of 232 mm × 16mm × 0.3mm, which was meshed by 8160 S4R-type elements, as shown in Fig. 4(a). The average mesh size is 3mm, such that 60 elements are distributed along the height of the blank. One driving roller, one feed roller, and two guide rollers were located around the blank and all of these rollers are rigid bodies. For the purpose of improving the calculation efficiency, the mass amplification factor is selected as 5000. The forming paths of each pass are shown in Fig. 1(b), which is identical to the experiment. More details of the FE model setup can be found in [5,19].
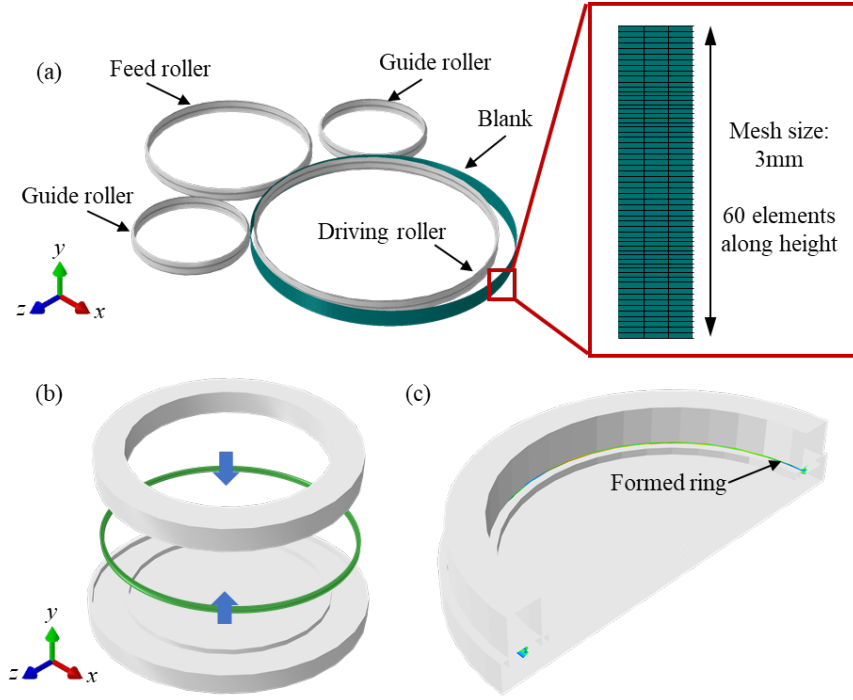
**Fig. 4.** FE model of the W-shaped metallic rings from (a) manufacturing to (b,c) service process.

After the sealing ring was formed, it was transferred to the supporting plate and compressed by a circular punch to mimic the service conditions as shown in Fig. 4(b) and (c). The movement of the punch was displacement-controlled and consisted of the preload part and fatigue part as sketched in Fig. 5. The displacement increased linearly from contact with the ring and reached the target value $u$ (i.e. the preload displacement) within 5 s. Then fatigue under a given frequency with the amplitude of 0.01 mm with respect to $u$ was applied on the punch. The stress history from the manufacturing to service at the trough of the rings, where cracks were observed experimentally [18], can be extracted for further analysis.
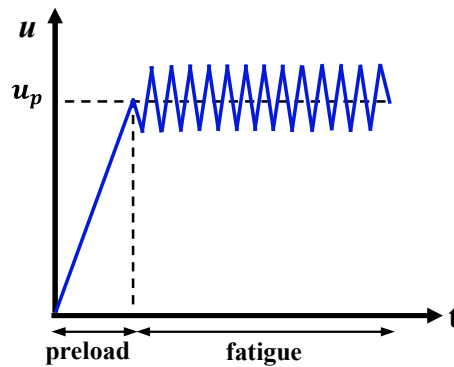


**Fig. 5.** Displacement-controlled loading applied on the punch during the service.

● Crystal plasticity finite element modeling

The GH4169 superalloy for manufacturing W-shaped metallic sealing rings has a face-centered cubic (FCC) structure with 12 $\{111\}\langle 1\bar{1}0\rangle$ slip systems to be potentially activated during plastic deformation. The constitutive slip rule to calculate the slip rate on each slip system is dislocation-based and, therefore, lengthscale-dependent. The crystal plasticity slip rule was numerically implemented into the ABAQUS-UMAT (User Material Subroutine).

The average dislocation velocity at a low strain rate regime related to the manufacturing and service of metallic rings is mainly governed by the thermally-activated escaping event from the pinned obstacles [28]. The total deformation gradient $\boldsymbol{F}$ consists of the elastic part $\boldsymbol{F}^e$ accounts for the rigid body rotation and the plastic part $\boldsymbol{F}^p$ accounts for the slip of all the slip systems, given by

$$\boldsymbol{F} = \boldsymbol{F}^e \boldsymbol{F}^p \tag{1}$$

The plastic deformation gradient is calculated according to the kinematics of deformation by

$$\dot{\boldsymbol{F}}^p = \boldsymbol{L}^p \, \boldsymbol{F}^p \tag{2}$$

where $\boldsymbol{L}^p$ is the plastic velocity gradient, which considers the contributions from all active slip systems given as

$$\boldsymbol{L}^p = \sum_{i=1}^{12} \dot{\gamma}^{(i)} \, \boldsymbol{s}^{(i)} \otimes \boldsymbol{n}^{(i)} \tag{3}$$

in which $\boldsymbol{s}^{(i)}$ and $\boldsymbol{n}^{(i)}$ is the unit vector which represents the slip direction and plane normal of system $i$, respectively. The slip rate $\dot{\gamma}^{(i)}$ used in the present study was first introduced by Dunne et al. [29], considering both forward and backward dislocation jump from pinned obstacles. The slip rule is expressed as

$$\dot{\gamma}^{(i)} = \rho_m b^2 \nu_D \exp\left(-\frac{\Delta F}{kT}\right) \sinh\left[\frac{\left(\tau^{(i)} - \tau_c^{(i)}\right) \Delta V}{kT}\right] \tag{4}$$

where $\rho_m$ is the average mobile dislocation density, $b$ is the Burgers vector, $\nu_D$ is the Debye frequency, $k$ is the Boltzmann constant and $T$ is the temperature. $\tau^{(i)}$ and $\tau_c^{(i)}$ are the resolved shear stress and corresponding critical value (CRSS) for slip system $i$. The activation energy $\Delta F$ and activation volume $\Delta V$ control the strain rate sensitivity of the material.

The evolution of dislocation density affects the CRSS and is reflected as the hardening behavior during deformation. The density of statistically stored dislocations (SSDs) is accumulated with plastic strain given by

$$\dot{\rho}_{SSD} = \gamma_{st}\dot{p} \tag{5}$$

The geometrically necessary dislocations (GNDs) can be computed by Nye's dislocation tensor as

$$\text{curl}(\boldsymbol{F}^p) = \sum_i \boldsymbol{b}^{(i)} \otimes \boldsymbol{\rho}_{GND}^{(i)} \tag{6}$$

The lattice curvature generated during plastic deformation is accommodated by the evolution of GND density and from which the lengthscale effect is accounted. The increase of SSD and GND densities contributes to the evolution of CRSS according to

$$\tau_c^{(i)} = \tau_{c0} + Gb\sqrt{\rho_{SSD} + \rho_{GND}} \tag{7}$$

in which $\tau_{c0}$ is the initial CRSS at the strain-free state and $G$ is the shear modulus of the superalloy.

In the present study, three CPFE models with the same slip rule and material parameters but different grain morphologies were established. The first one was replicating the real microstructure based on the EBSD map of the uniaxial tensile sample and was used to calibrate the modeling parameters. The second one was replicating the initial microstructure around the crack site in the three-point bending sample in order to determine the threshold for crack nucleation in the superalloy. The grains of both models were extruded along the thickness direction. The third model was constructed using three-dimensional Voronoi tessellations with the same average grain size as the experimental measurement since the deformation histories along all three directions from manufacturing to service were considered and applied as the boundary conditions. The crystallographic orientations of all these models were assigned based on EBSD characterizations.

## 3. Determination of the critical stored energy for fatigue crack initiation in GH4169 superalloy

### 3.1 Calibration of modeling parameters

To accurately capture the rate-dependent responses of the superalloy, an area of $194\mu m \times 162\mu m$ was selected from the EBSD map of the gauge section of the tensile sample to construct the CPFE model with a thickness of $10\mu m$, as shown in Fig. 6. The initial microstructure of the material mainly consists of equiaxed grains and a few twin grains. The average grain size is about $20\mu m$ and the material is slightly textured with a maximum intensity of 1.40. The model was meshed by 73260 reduced integration C3D20R elements. The left, bottom and back surface was constrained along the x-, y- and z-direction, respectively. Displacement-controlled loading was applied on the right surface as illustrated in Fig. 6(c).
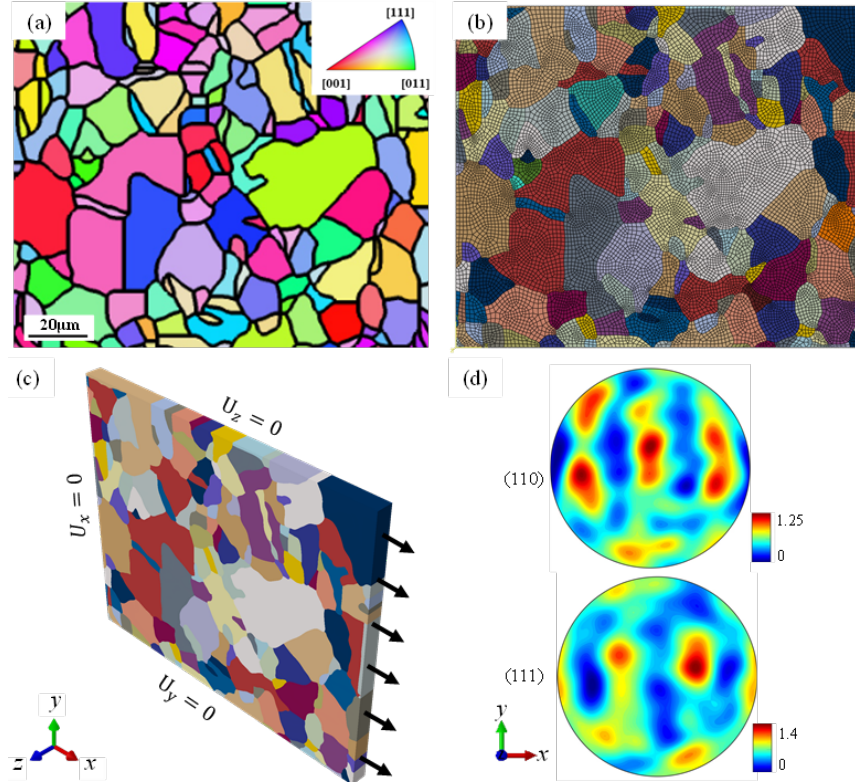


**Fig. 6.** The CPFE model based on the real microstructure. (a) EBSD map within the gauge section of the tensile sample; (b) morphology of the CPFE model which replicates the grain morphology; (c) boundary conditions, and (d) pole figures of the model.

The initial CRSS, activation energy and volume was calibrated against the experimental data to capture the yield point and strain rate sensitivity of the material. Other parameters in the model were chosen from the literature [30–34] that represents the nickel-based superalloys. The computed stress-strain curves show reasonably good agreement with the experiment, as shown in Fig. 7 and the modeling parameters are summarised in Table 2.

It is worth noting that a pseudo-3D microstructure based on the surface EBSD map was used for calibrating the CPFE parameters. It is well known that the sub-surface grains have an effect on the mechanical behaviors of materials at different degrees depending on the microstructure. The 3D statistically equivalent virtual polycrystalline microstructures has been introduced and can be used for calibrating. This method has specific advantages and has been demonstrated its applicability in dealing with complex and heterogeneous microstructures [35–39]. In the present work, the GH4169 superalloy consists of a relatively simple microstructure with mainly equiaxed grains and near-random textures. Therefore the effect from the sub-surface grains on the mechanical behaviors is believed to be negligible if sufficient grains were included in the model of calibration. The two different types of CPFE models (pseudo-3D microstructure and 3D Voronoi tessellations) used in this work are able to capture the macroscopic mechanical responses of the material as demonstrated in Appendix A.
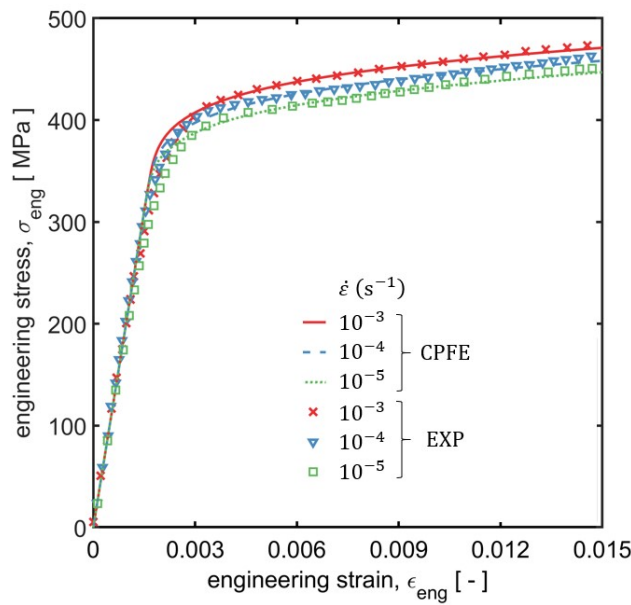


**Fig. 7.** Calibration of the stress strain responses under different strain rates.

**Table 2.** Modeling parameters for GH4169 superalloys

| parameter (unit) | value | parameter (unit) | value |
|---|---|---|---|
| $\tau_{c0}$ (MPa) | 152.00 | $b$ (μm) | $3.50 \times 10^{-4}$ |
| $\Delta F$ (J) | $11.00 \times 10^{-20}$ | $G$ (GPa) | 79.60 |
| $\Delta V$ (-) | $62.86 b^3$ | $\gamma_{st}$ (-) | 48.00 |
| $\nu_D$ (Hz) | $1.00 \times 10^{11}$ | $k$ (J · K$^{-1}$) | $1.38 \times 10^{-23}$ |

| $T$ (K) | 293.00 | $\rho_m$ ($\mu m^{-2}$) | 5.00 |
|---|---|---|---|

## 3.2 Fatigue crack initiation in GH4169 superalloys

In the quasi-in-situ three-point bending experiment, crack nucleation was observed to occur between 8000-8500 cycles. EBSD characterization was carried out around the crack at the end of 8500 cycles without additional polishing. Based on the deformed microstructure, the region around the crack before fatigue can be identified and a 124.8μm × 94.9μm sized area was selected as the region of interest (ROI) as shown in Fig. 8, where the arrows indicate the location of the crack.

Using the three-point bending macroscopic FE model in Section 2.2, the normal stresses along three directions were calculated as shown in Fig. 9. A crack was observed at the bottom center of the beam, where the material was subjected to uniaxial tensile stress along the x-direction as demonstrated in Fig. 9(b). The peak stress is 683MPa and the stress ratio is $R = -0.5$. A CPFE model was constructed using the identical grain morphology and crystallographic orientations as the EBSD map of ROI before deformation. The extracted local stress history from the FE model was applied as the boundary conditions of the CPFE model, as illustrated in Fig. 10.
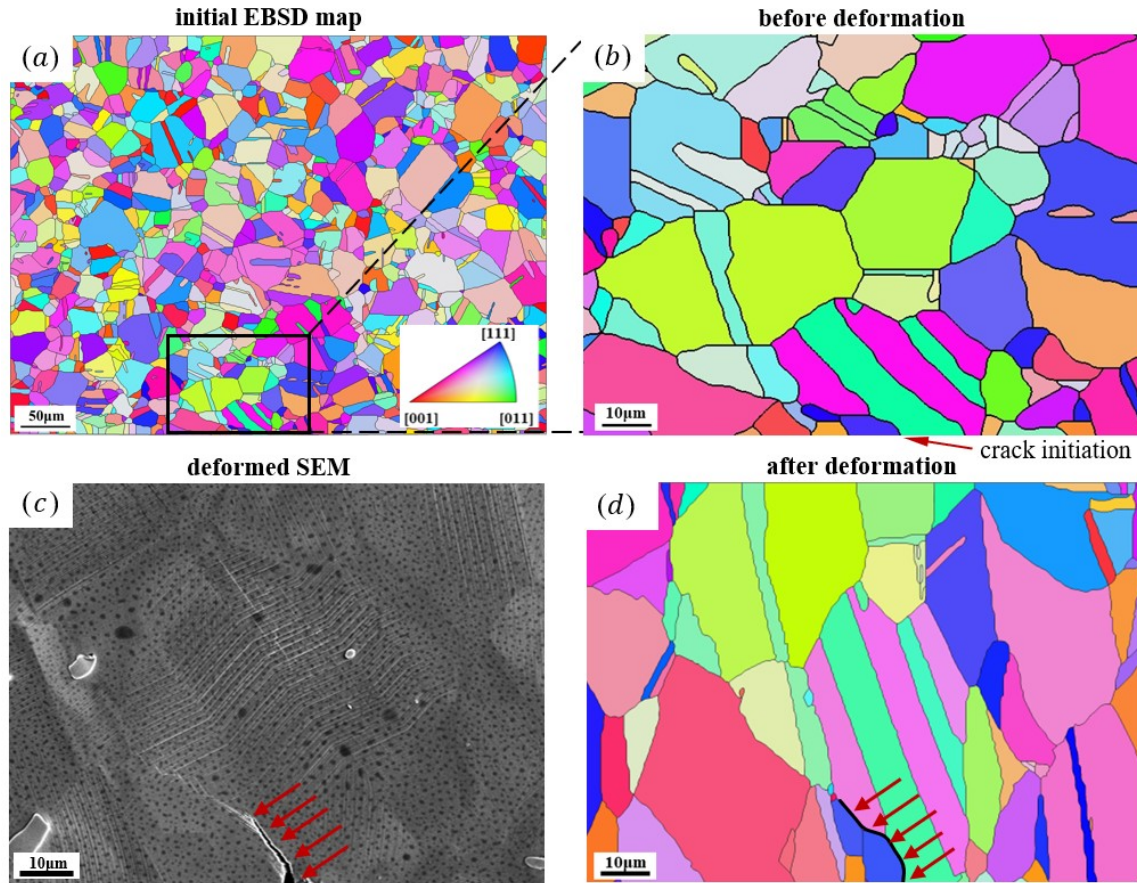


**Fig. 8.** Crack nucleation under the three-point bending fatigue loading. (a) EBSD map before deformation; (b) magnified map near the region of cracking; (c) SEM image show the crack morphology taken at the end of 8500 cycles; and (d) EBSD map after cracking where the arrows indicate the location of the crack.
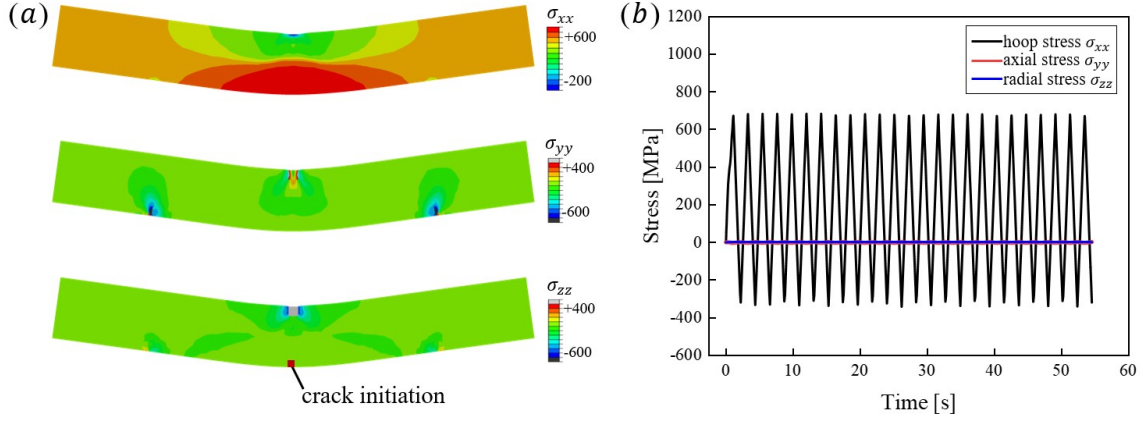
**Fig. 9.** Stress distribution computed by the three-point bending FE model. (a) stress distribution of each component; (b) evolution of stress componenet at the ROI.
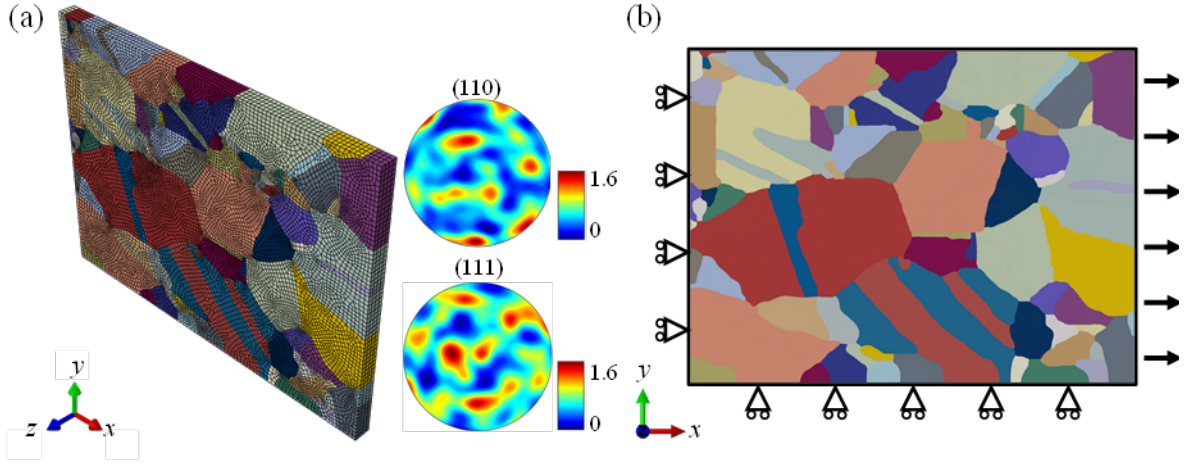


**Fig. 10.** The CPFE model of ROI. (a) mesh and pole-figures; (b) boundary conditions.

Under the cyclic loading, inhomogeneous plasticity was developed within the crystal. In order to quantify the fatigue life to crack nucleation, a stored-energy-density-based criterion is used in this study. The stored energy density was first introduced by Wan et al. [40] to predict fatigue crack nucleation in polycrystals. The stored energy density increasing rate (per cycle) is calculated as

$$\dot{G} = \int \frac{\xi |\boldsymbol{\sigma}{:}\mathrm{d}\boldsymbol{\varepsilon}^p|}{\sqrt{\rho_{SSD} + \rho_{GND}}} \tag{8}$$

where $\xi = 5\%$ is the empirically accepted fraction of energy stored in the material. It is argued that there is approximately 5% energy stored in the dislocation structure during plastic deformation while the remaining 95% is dissipated as heat [41]. Using this stored energy density as a criterion, the fatigue crack nucleation [31,32], and path deflections and growth rate during the subsequent crack propagation [42–45] can be well captured in various engineering alloys. More importantly, the stored energy density has been proved to be the primary driving force for crack nucleation, while the other quantities, such as local stress, slip activity, and GND density, are necessary but not sufficient to predict all the experimentally observed cracks [32]. The mechanistic explanation of the stored energy density has also been elucidated using discrete dislocation plasticity modeling [30,46]. The proposed dislocation configurational energy density stored in the dislocation structure is fundamentally related to the stored energy density, which is argued to be a key mechanistic factor in fatigue crack nucleation and growth. Therefore, in the present work, the stored energy density is used as the main driving force

for cracking in the GH4169 alloy and its critical value was determined by integrating the three-point bending experiment and modeling.

Fig. 11 shows the crack nucleation site and the predicted distribution of stored energy density in the corresponding region. The highest stored energy density point at the end of 100 fatigue cycles in the CPFE model was observed near the bottom of the polycrystal as labeled by 'P' in Fig. 11(b), which coincides with the experiment crack location in Fig. 11(a). There are other 'hotspots' of the stored energy density in Fig. 11(b) as well, but the magnitude at these locations is lower than that at position 'P', which can be treated as potential secondary crack nucleation sites. Note that by only calibrating the macroscopic rate-dependent plastic behavior of the superalloy, the established CPFE model is able to precisely capture the crack nucleation site at the microstructure lengthscale. The evolution of stored energy density along the A-A' path in Fig. 11(b) was extracted as shown in Fig. 11(c). The concentration of stored energy density was observed clearly in the region of crack nucleation.
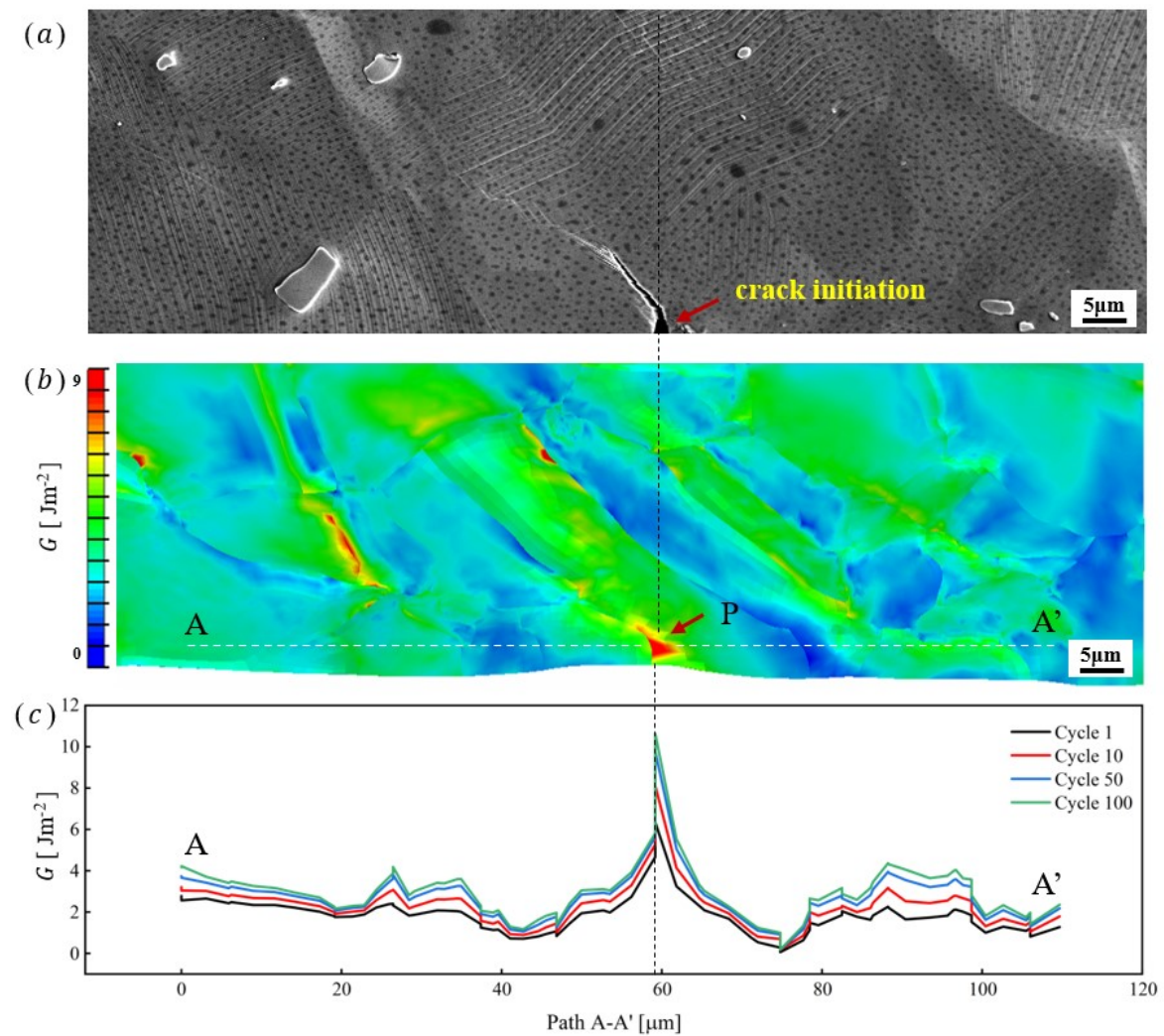


**Fig. 11.** The stored energy around the crack. (a) morphology the crack; (b) spatial distribution of the stored energy density at the end of 100 cycles; (c) evolution of stored energy with cycles along the A-A' path as shown in (b).

The concentration of the stored energy density observed in Fig. 11 was due to the establishment of dislocation pile-ups against the grain boundary due to the inhomogeneous plastic deformations. Fig. 12 shows the evolution of dislocations around the crack nucleation site at different loading cycles.

The two neighboring grains on both sides of the crack have different crystallographic orientations as illustrated by the cubic units in Fig. 12. Plastic heterogeneity was established within these grains at the early stage of fatigue. High dislocation density can be observed near the grain boundary as a result. With further loading cycles, more dislocations piled up against the boundary and thus, more energy is stored in the dislocation structure. The stored energy density resulting from dislocation pile-ups evolved with loading cycles and is argued to drive cracking eventually.
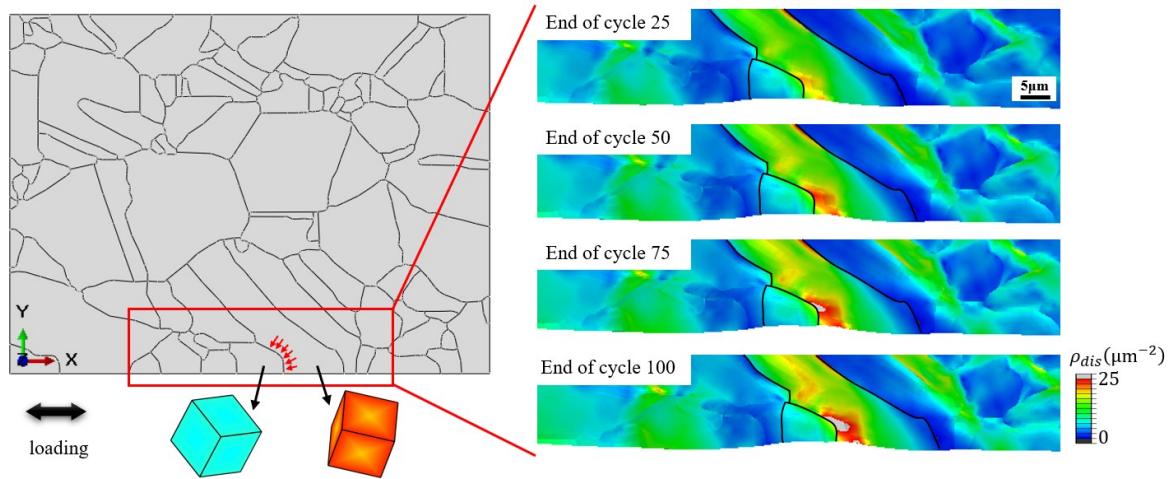


**Fig. 12.** Evolution of the dislocation density with cycles around the crack nucleation site. The red arrows indicate the location of the experimentally observed crack. Different crystallographic orientations of the neighboring grains induced plastic heterogeneity and dislocation concentration at the grain boundary under fatigue loading.

The evolution of local stored energy density at point 'P' is quantified and presented in Fig. 13. It is found that the energy density increases rapidly at the onset of plastic deformation and the rate of increase is gradually reduced with cycles. The development of the local energy density is stabilized after about 50 cycles, from which the trend of stored energy density increasing is extracted as a linear function given by

$$G = 1.01 \times 10^{-2} N + 5.61 \tag{9}$$

where the unit of energy density is $Jm^{-2}$ and $N$ is the number of fatigue cycles. Since crack was found to nucleate between 8000-8500 cycles, the stored energy density at 8250 cycles is extracted as the threshold for fatigue crack nucleation in GH4169 superalloys. The determined value is 88.9 $Jm^{-2}$, with the uncertainty of 2.525 $Jm^{-2}$ (equivalent to the energy density increase within 250 cycles). This value is then applied to assess the fatigue life of GH4169 metallic sealing rings.
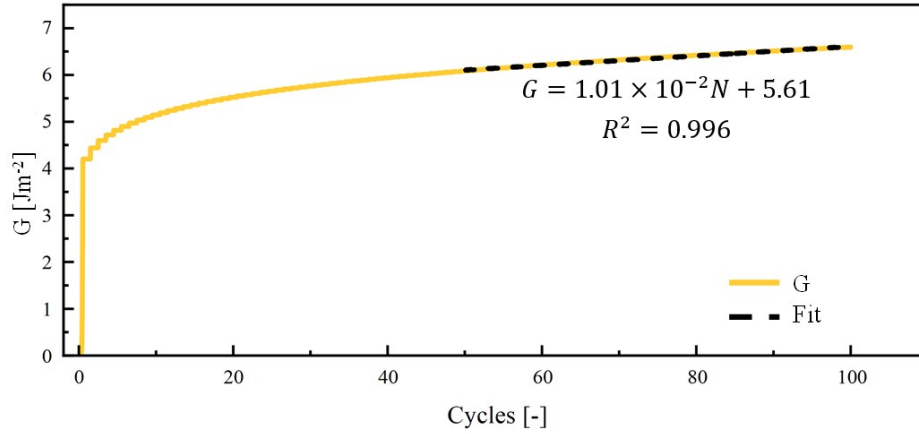
$$G = 1.01 \times 10^{-2}N + 5.61$$
$$R^2 = 0.996$$

**Fig. 13.** The evolution of the stored energy density at location 'P' where crack nucleation was observed.

## 4. Macro- and micro-deformation behaviors of metallic sealing rings from manufacturing to service

### 4.1 Fatigue responses under the typical forming and service condition

In order to comprehensively consider the deformation experienced by the material from the multi-pass rolling forming to the fatigue operation, the hoop stress and axial stress at the trough of the rings, where the crack was experimentally observed during service [18], are extracted from the macroscopic FE model, as plotted in Fig. 14. The forming process consists of five passes rolling, as illustrated in Fig. 1(b) [5]. The investigated W-shaped metallic sealing ring is mainly used in aero-engines and the service conditions are preloaded to $u = 0.2$-$0.4$ mm, vibrate at the frequency of $f = 0.33$-$1.00$ Hz and the pressure $p$ of the sealed medium is between 1.0-3.0 MPa [47]. Hence, a typical condition of $u = 0.3$ mm, $f = 0.50$ Hz and $p = 2.0$ MPa is chosen to understand the fatigue responses of the rings from manufacturing to service, followed by a systematic investigation of the influence from each service parameters on the fatigue life.
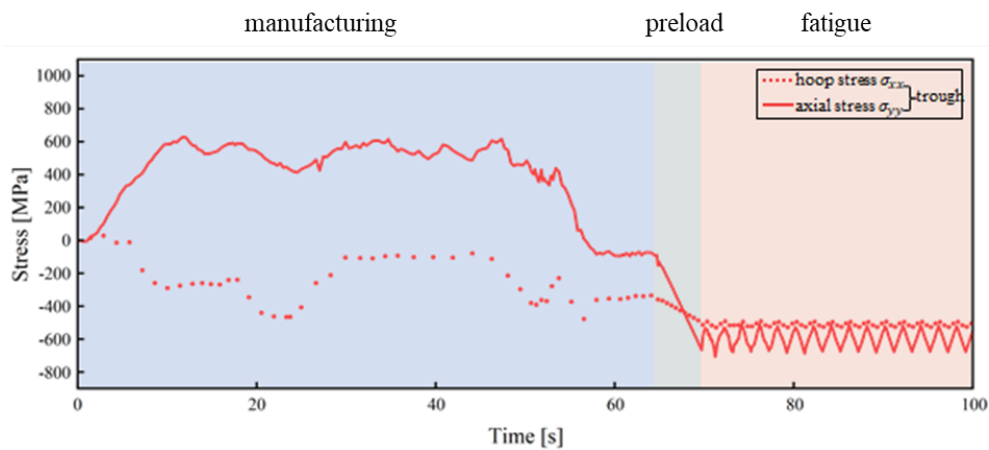


**Fig. 14.** Evolutions of the hoop stress and axial stress at the trough of the rings from manufacturing to service.

It is clearly shown in Fig. 14 that the material is subjected to complex multiaxial stress history during the whole process. The hoop stress is always compressive and the magnitude is higher in the fatigue stage. However, the axial stress changes from tensile to compressive with a similar magnitude of

~600MPa from manufacturing to service. The resolved shear stress on the slip systems is expected exceed the critical value (152MPa as in Table 2) resulting from these high stresses and thus the material has been plastically deformed before the preload stage. The establishment of the dislocation structure and the corresponding accumulation of the stored energy during the manufacturing stage would significantly affect the service life of the rings.

It is worth noting that, in the present study, the worst case is considered where no heat treatment was involved in the process. For some specific types of metallic sealing rings, an annealing treatment is required before they are put into service. In such a scenario, the changes in the dislocation structure and stored energy density during the heat treatment must be taken into consideration as well. Although the residual stress and dislocation density are noticeably reduced during the annealing, for the majority types of the rings, the material state cannot be recovered to the same state as the raw sheet before rolling. Therefore, the deformation history before service cannot be ignored when evaluate the fatigue life of the components.

To account for the complex multiaxial stress history, a CPFE model was established with the grain morphology generated by 3D Voronoi tessellations. The hoop stress and axial stress extracted from the FE model as shown in Fig. 14 were applied on the right ($\sigma_{xx}$) and top ($\sigma_{yy}$) surfaces, respectively, while the left, bottom and back surfaces were constrained along x-, y- and z-direction, respectively, as depicted in Fig. 15. Since the variations of the stress in both directions are strong, a maximum time step of 0.01 s was employed in the CPFE model to accurately resolve the loading history. The model consists of 64 grains and is meshed by 13955 C3D10 elements. The crystal orientations of the grains were assigned according to the EBSD data such that the overall texture of the CPFE model is representative of the materials.
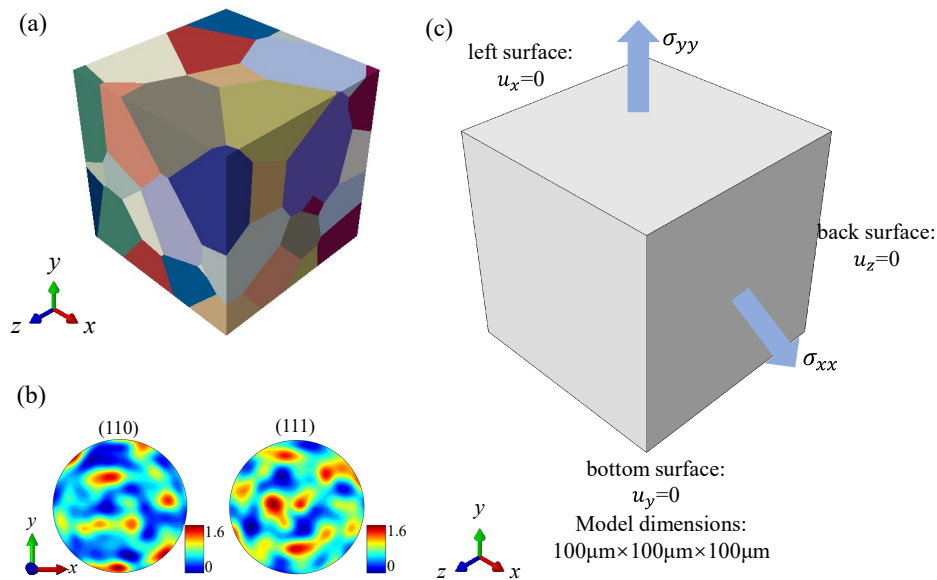


**Fig. 15.** 3D CPFE model constructed using 3D Voronoi tessellations. (a) grain morphology; (b) pole figures and (c) loading conditions.

Under the typical forming process and service condition, plasticity has been introduced in the crystal and the localized plastic deformation induces the high stored energy density, which serves as the driving force for potential crack nucleation. In particular, at the location 'Q' in Fig. 16(a), the highest energy density was found at the quadruple junctions of the grain boundaries of grain labeled by 37, 53, 55, and 63. Within these four grains, Grain 53 is oriented preferentially for slip under the given

loading conditions, while the rest are hard to deform. As shown in Fig. 16(c) and (d), dislocations were moving towards the grain boundary and caused localized plastic deformation. The neighboring grains did not produce sufficient plastic strain to release the local stress concentration. Arising from the highly-dense dislocation structure near the quadruple junctions, high stored energy density occurred at the same location as shown in Fig. 16(e).
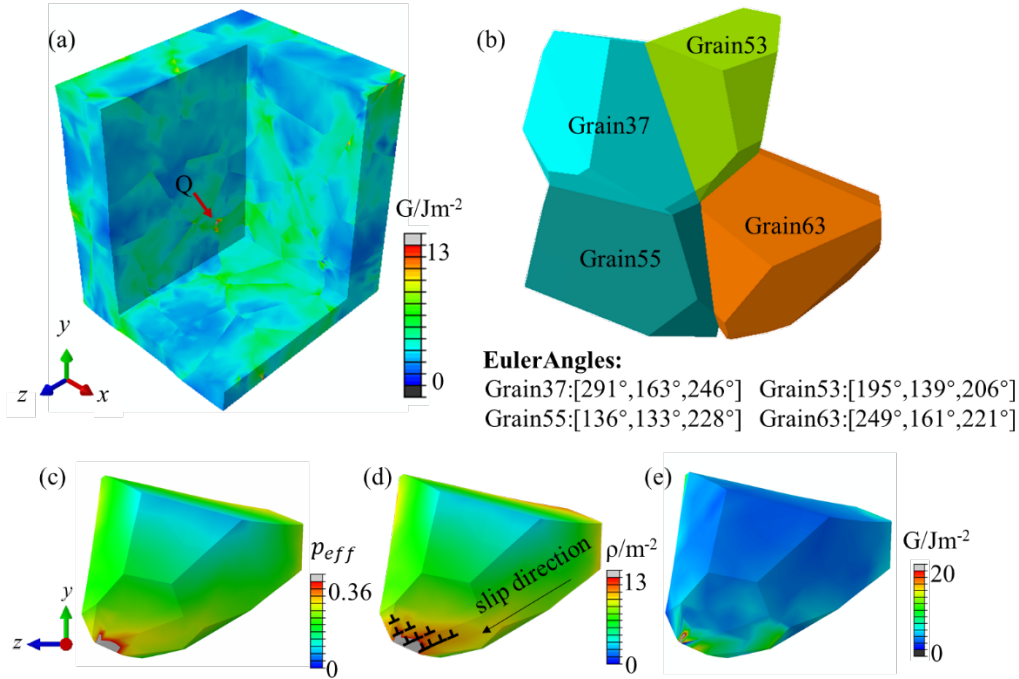


**Fig. 16.** (a) Stored energy distribution predicted by the CPFE model; (b) schematics of the four grains around the location with the highest stored energy density. Distributions of (c) effective plastic strain, (d) dislocation density, and (e) the stored energy density of Grain 53 at $t = 100$ s.

The accumulation of stored energy density at point 'Q' is plotted in Fig. 17. It is found that the stored energy gradually increases during different passes of the rolling and the amount of energy accumulation differs from each other. By the end of the manufacturing of the sealing ring, 4.4 Jm$^{-2}$ stored energy density has already been established, which occupies ~5% of the threshold for cracking. During the subsequent preload and the first five fatigue cycles, the stored energy density is further increased. After the first five cycles, the stored energy density evolves approximately linearly with time $t$ given by

$$G = 2.26 \times 10^{-2}t + 3.00 \qquad (10)$$

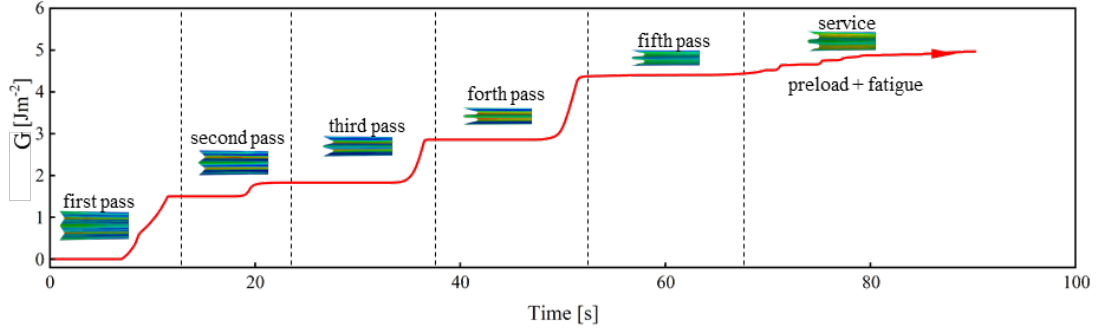and from which the service life can be estimated as 1866 cycles.

**Fig. 17.** Evolution of the stored energy density at the point 'Q' as in Fig. 16(a).

It is worth noting that the stored energy accumulated during the manufacturing not only contributes to the total energy before failure but also affects the rate of stored energy density development during service. To emphasize this statement, we consider another two scenarios for comparison, i.e. (1) completely ignore the loading history during manufacturing and only consider the preload and fatigue stages; and (2) estimate and apply the average stress of the forming process while considering the same service profile as in Fig. 14. The highest stored energy density for these two scenarios is extracted and compared with the manufacturing-to-service fully considered case in Fig. 18. It is observed that without considering the deformation history during manufacturing, the accumulation of stored energy density is much lower. The stable evolution rate of the stored energy density is also lower compared to the fully considered case. Hence, the fatigue life would be over-estimated if the contribution of the manufacturing process is not appropriately considered.
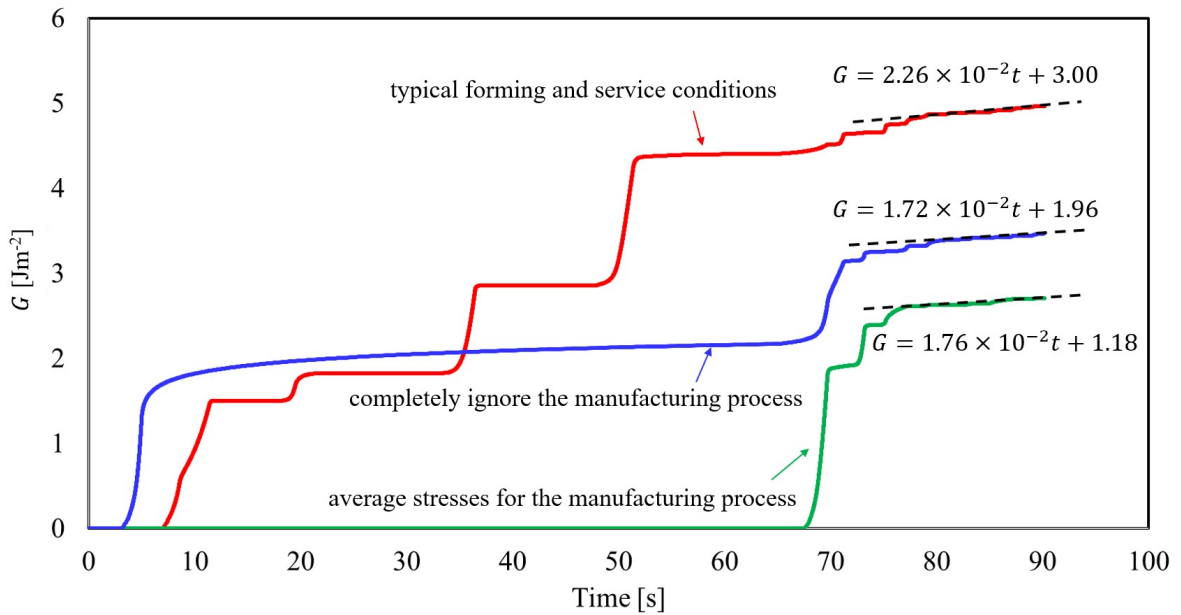


**Fig. 18.** Evolution comparison of the stored energy density.

## 4.2 Effect of service parameters on the fatigue life of metallic sealing rings

Based on the above analysis, it can be concluded that the manufacturing process is important in determining the fatigue life of the W-shaped metallic rings. However, only the typical service condition is considered, and the operational environment may change. To systematically investigate

the effect of different service parameters and evaluate the corresponding life, the parameters listed in Table 3 are considered sequentially.

**Table 3.** Service parameters of W-shaped metallic sealing rings

| Service parameters | Values |
|---|---|
| Preload $u$ (mm) | 0.20, 0.25, **0.30**, 0.35, 0.40 |
| Pressure $p$ (MPa) | 1.0, 1.5, **2.0**, 2.5, 3.0 |
| Frequency $f$ (Hz) | 0.33, 0.40, **0.50**, 0.67, 1.00 |

● Effect of preload

In considering different service conditions, the local stress history at the trough is also changing. Fig. 19(a) shows the multiaxial stress for two different preloads. Both hoop stress and axial stress are affected by the preload, and the magnitude of which increases with the preload. It can be seen in Fig. 19(b) that the magnitude of the hoop stress and axial stress becomes similar when the preload is large, i.e. the stress biaxially defined by $\sigma_{xx}/\sigma_{yy}$ reduces to 1 when the preload increases from 0.20 to 0.40 mm. In addition, during the fatigue stage, the stress ratio of the axial direction reduces with the preload while the value of the hoop direction is barely affected.

The changes in the local stress history would affect the stored energy density evolution. Fig. 20(a) is the computed evolution of stored energy density in the service stage under different preloads. The amount of energy accumulation during the preload and early fatigue cycles is higher when a large preload is prescribed. The plastic deformation and its inhomogeneity are enhanced when the preload is large. More importantly, the evolution rate of stored energy density is also increased with the preload, which implies a shorter fatigue life. In this case, the sealing performance may be better, but the component is expected to fail much earlier. Fig. 20(b) presents variations of the stored energy density evolution rate extracted from the stable increasing stage in Fig. 20(a) and the corresponding fatigue life calculated using the determined threshold for crack nucleation. It can be seen that when the preload increases from 0.2 to 0.3 mm, the service life reduces by about one order of magnitude. With the further increase to 0.4 mm, the fatigue life is below 1000 cycles which suggests that the sealing ring could not satisfy the safety requirement of the engine. Additional treatment is thus needed for these service conditions.
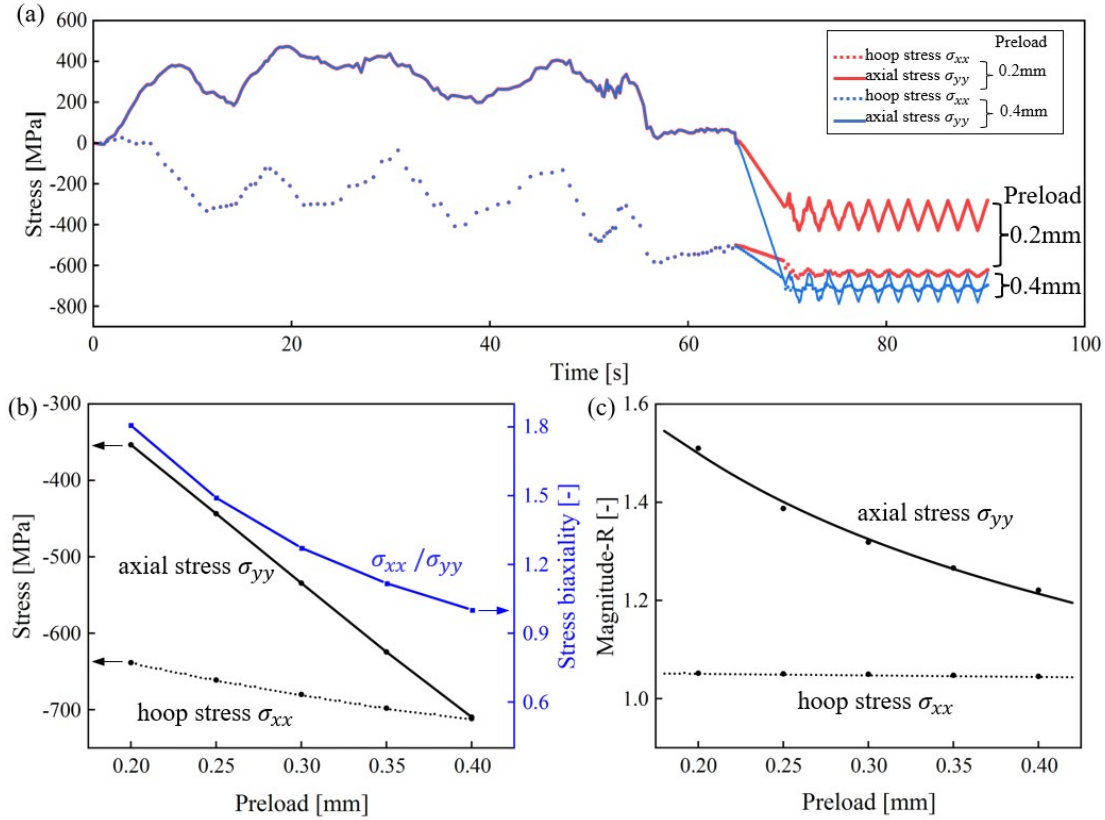
**Fig. 19.** The effect of preload on the local stress at the trough. (a) stress history along the hoop and axial directions; (b) stress biaxiality, and (c) stress ratio R for different preload.
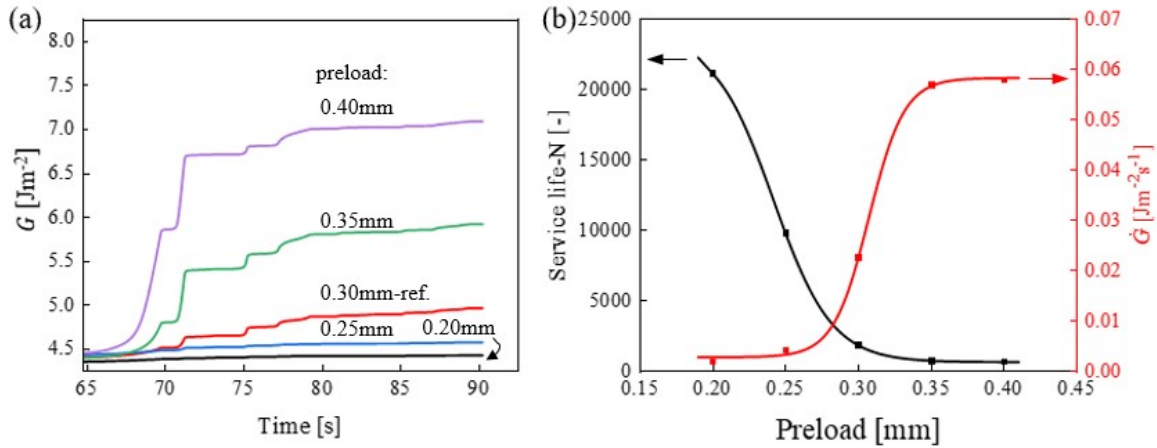


**Fig. 20.** (a) Evolution of the stored energy density, and (b) fatigue lives under different preloads.

- Effect of the sealed medium pressure

To seal different mediums during the service, the pressure act on the sealing ring may change. Generally, the pressure of the sealed medium varies between 1.0 to 3.0 MPa. By changing the related setup in the FE model, the local stress at the trough also varies as shown in Fig. 21. Both magnitudes of hoop stress and axial stress increase with pressure while the stress biaxiality increases slightly. The dependence of the stress ratio along the hoop and axial directions with the pressure is not significant, although a decreasing trend needs to be acknowledged.
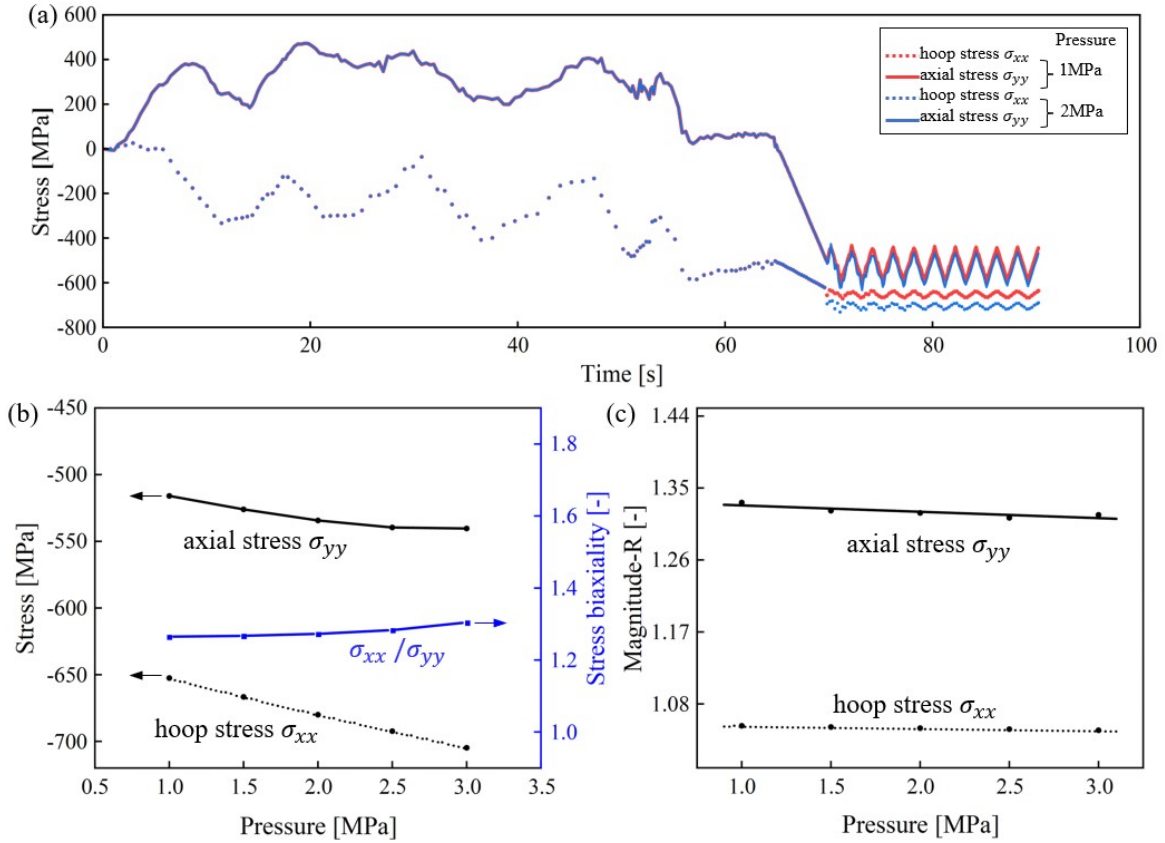
**Fig. 21.** The effect of pressure on the local stress at the trough. (a) stress history along the hoop and axial directions; (b) stress biaxiality, and (c) stress ratio R for different pressures.

The stress history was then applied as the boundary conditions for the CPFE model and the evolution of the highest stored energy was then extracted. As shown in Fig. 22(a), the magnitude of the stored energy density increases with the pressure and the stabilized evolution rate is similar to each other. The evolution rate of stored energy density and the corresponding fatigue life are quantitatively compared in Fig. 22(b). The higher pressure of the sealed medium makes the sealing rings sustain higher stress conditions. Therefore, the peak stored energy density reaches the threshold earlier and the fatigue life is thus shorter.
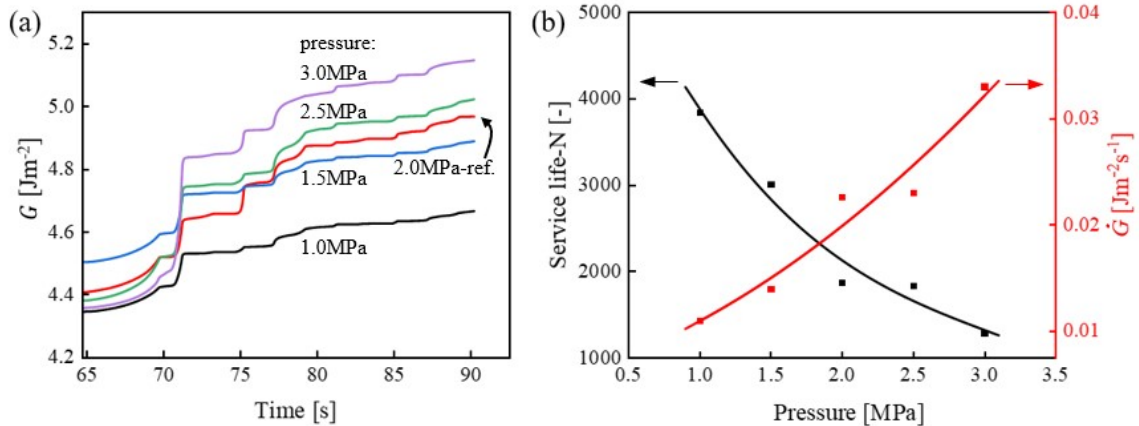


**Fig. 22.** (a) Evolution of the stored energy density, and (b) fatigue lives under different pressures.

● Effect of vibratory frequency

Even for the same sealed medium and identical preload conditions, the frequency of the relative vibratory motion of adjacent pipes may change due to different operational environments. As a consequence, the fatigue frequency can be different. Here, the effect of frequency between 0.33-1.00 Hz is considered. As shown in Fig. 23, except for the stress rise and fall time of each loading cycle, the stress history, including the magnitude of each stress component, stress biaxiality and stress ratio, is not affected by the frequency.

The evolutions of the highest stored energy density in the CPFE under different fatigue frequencies are plotted in Fig. 24(a). It is observed that the rate of accumulation is faster when the frequency is higher, which is attributed to the short time of each cycle. As demonstrated in Fig. 24(b), the evolution rate (with respect to time) increases linearly with frequency. It appears that for a given period of time, increasing the stress oscillations would accelerate the establishment of dense dislocation structure and thus promote the accumulation of stored energy. This is fundamentally related to the strain rate sensitivity of the GH4169 superalloy, in which the motion of dislocations is significantly affected by the stress rate of the remote loading [48]. The increase in fatigue frequency provides more chances for dislocations to move backward and forward and interrupt the stable configuration. Therefore the thermally activated escaping from the pinned obstacles is enhanced and the pile-ups against grain boundaries are stronger. Based on the computed stored energy density, the fatigue life of the metallic sealing rings shows a parabolic relationship to the vibratory frequency as in Fig. 24(b). It is worth noting that the fatigue life in Fig. 24(b) is shown in the number of cycles which is consistent with the previous analysis. However, due to the change in fatigue frequency, the time to fatigue crack nucleation in fact reduces with the increase in frequency.
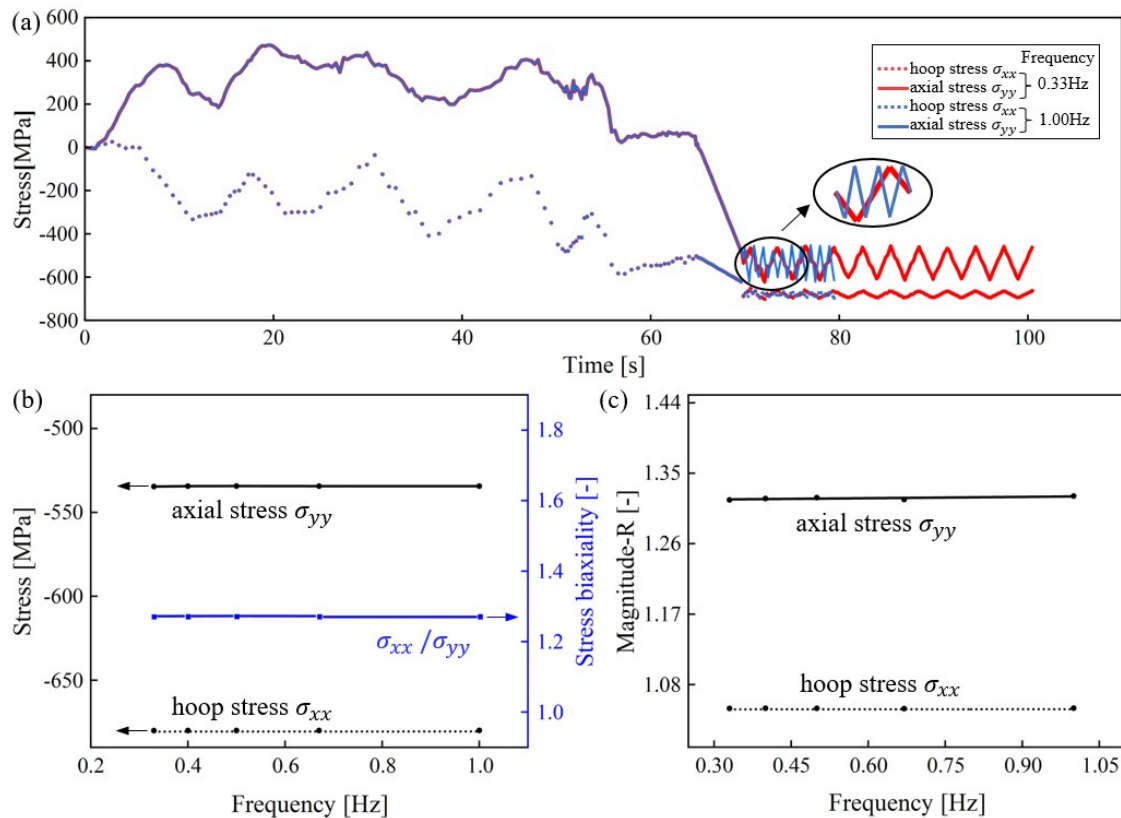


**Fig. 23.** The effect of frequency on the local stress at the trough. (a) stress history along the hoop and axial directions; (b) stress biaxiality, and (c) stress ratio R for different frequencies.
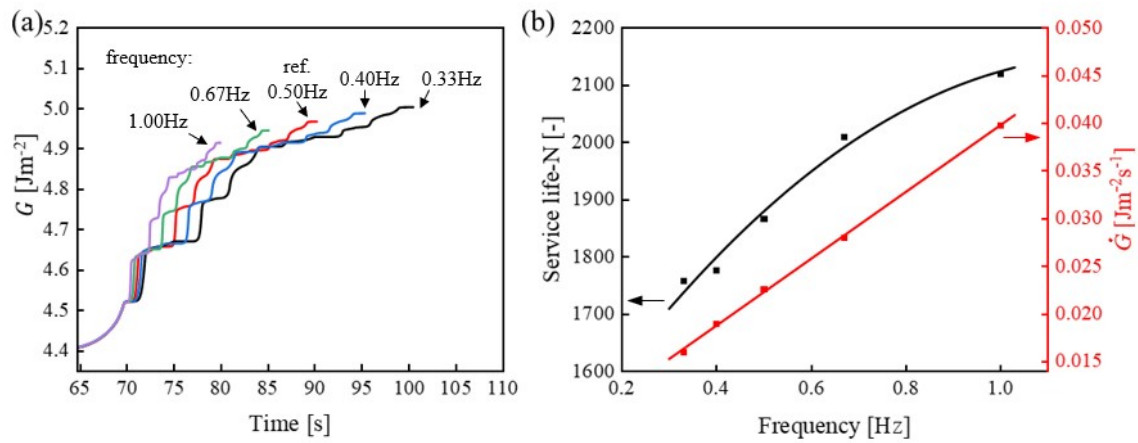
**Fig. 24.** (a) Evolution of the stored energy density, and (b) fatigue lives under different frequencies.

## 4.3 Discussions

It has been demonstrated that the deformation history during manufacturing must be considered to assess the fatigue life of the metallic sealing rings, as it not only determines the initial state of the material that will be subjected to cyclic loading but also affect the energy accumulation rate during the subsequent service stage. Macroscopically, for the GH4169 nickel-based superalloy, positive strain rate sensitivity and strain hardening can be observed under room-temperature deformation. That leads to a strong dependence of the material properties of the rings on their deformation routes. In addition, the contribution of the manufacturing stage cannot be simply estimated using average stress since the deformation rate of the multi-pass rolling is typically non-uniform and fluctuant. Microscopically, the stored energy density that drives fatigue crack nucleation significantly depends on the dislocation structure evolutions. The initial configuration of the dislocation structure is formed during the rolling, and the development of the structure under fatigue is based on this initial configuration. That is the main reason for the overestimation of the fatigue life if the contribution of the manufacturing process is not appropriately considered.

The contribution of stored energy density during manufacturing is ~5% of the total energy density for cracking for the specific ring considered here. This percentage may vary with the geometry of the ring (e.g. distance between the crest and trough, diameters of the rings, etc.) and the forming methods (e.g. number of passes, feed ratio, etc.). Nevertheless, such contributions are equivalent to hundreds to thousands of fatigue cycles of the ring under service conditions.

After the macroscopic material state and dislocation structure was determined during manufacturing, the service conditions show effects on the fatigue life. Among all the three service parameters within the considered range, the preload has the most noticeable effect on the fatigue life of the rings as it not only influences the stored energy density during the preloading stage but also changes the baseline of the fatigue stresses. A larger preload introduces higher local stress at the trough. The dislocation pile-ups are thus denser, which may also be further condensed in the subsequent cycling. As a result, rapid energy accumulation and crack formation can be expected. On the contrary, the dependence of service life on the vibratory frequency is the weakest. The role of the fatigue frequency relies on the rate-dependent plasticity of the material. Although the GH4169 superalloy experiences a positive strain rate sensitivity at room temperature, its effect on the fatigue life is not large enough to overrun the effect of the applied stress. As for the moderate effect from the medium pressure, the plastic deformation localization is enhanced by higher pressure. Since the medium pressure is evenly distributed along 'W' shape of the ring which is different from the primary loading direction, its value

may change the local stress around the dislocation pile-ups and therefore affect the stored energy density evolutions. However, the sealing stress applied from the adjacent pipes is generally much higher than the medium pressure. The medium pressure thus only plays a secondary role in affecting the fatigue performance of the metallic sealing rings.

## 5. Conclusions

In this study, the fatigue crack nucleation in W-shaped metallic sealing rings is systematically studied by comprehensively considering the deformation history from manufacturing to service. The key outcomes are summarised as follows:

(1) The stored energy density criterion has been proved to be able to capture the location of crack nucleation in the GH4169 superalloy by integrating the three-point bending experiment and multiscale modeling. The critical value for fatigue crack nucleation is $88.9\ \mathrm{Jm}^{-2}$.

(2) Under a typical forming and service condition, the amount of stored energy density accumulated during manufacturing contributes ~5% of the total energy density for cracking.

(3) The deformation history during manufacturing not only influences the early-stage energy accumulation but also affects the evolution rate of energy density during the service. The fatigue life may be overestimated if the manufacturing process is not appropriately considered.

(4) The fatigue life of the W-shaped metallic sealing rings decreases with the increase in preload and the pressure of the sealed medium. While the number of cycles to crack increases with the vibratory frequency. Among these three parameters, the preload has the most significant effect on the fatigue crack nucleations.

## Acknowledgments

## Appendix A. Macroscopic mechanical responses of three crystal plasticity finite element models.

Three crystal plasticity finite element models were constructed based on the real microstructure of the uniaxial tensile sample (CPFE model 1) and the three-point bending sample (CPFE model 2) and three-dimensional Voronoi tessellations (CPFE model 3). All these models are able to capture the strain rate sensitivity of the GH4169 superalloy as shown in Fig. 25.
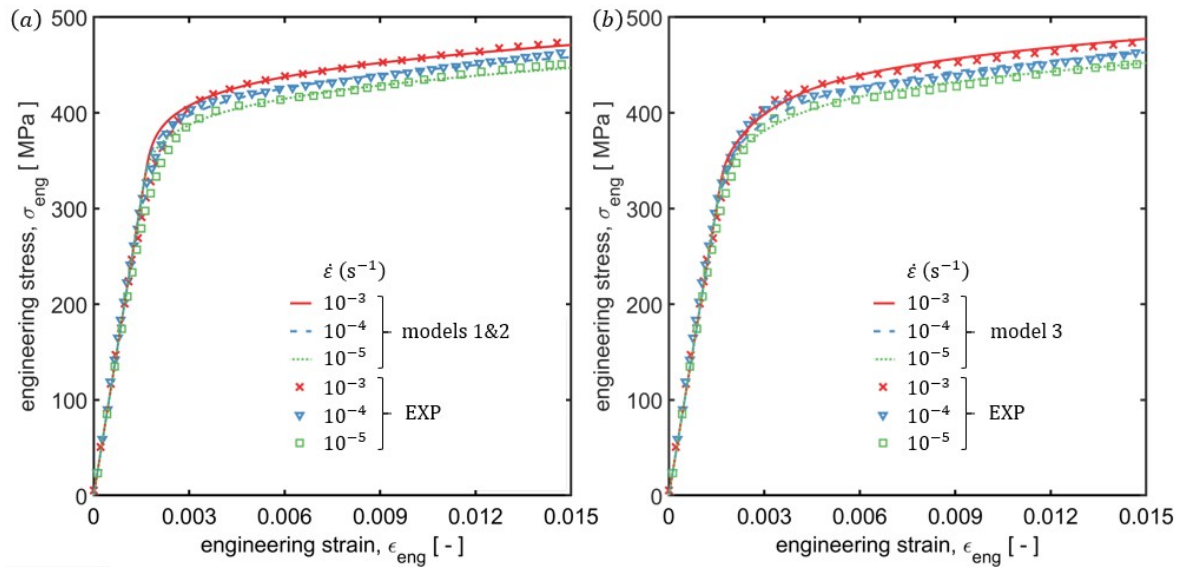
**Fig. 25.** Stress-strain curves of three CP models compared against the experimental measurement. Results from (a) CPFE models 1 and 2 (both have almost the same responses) and (b) CPFE model 3.

# References

[1]    Zheng Z, Zhan M, Fu MW. Microstructural and geometrical size effects on the fatigue of metallic materials. Int J Mech Sci 2022;218:107058. https://doi.org/10.1016/J.IJMECSCI.2021.107058.

[2]    Zheng Z, Zhao P, Zhan M, Shen S, Wang Y, Fu MW. The roles of rise and fall time in load shedding and strain partitioning under the dwell fatigue of titanium alloys with different microstructures. Int J Plast 2022;149:103161. https://doi.org/10.1016/J.IJPLAS.2021.103161.

[3]    Xu Y, Fox K, Rugg D, Dunne FPE. Cyclic plasticity and thermomechanical alleviation in titanium alloys. Int J Plast 2020:102753. https://doi.org/https://doi.org/10.1016/j.ijplas.2020.102753.

[4]    Ding XY. The Structure Optimization Design for the W-Type Metallic Sealing Ring Based on the MOGA Algorithm. Appl Mech Mater 2015;727–728:541–5. https://doi.org/10.4028/www.scientific.net/AMM.727-728.541.

[5]    Li L, Li Z, Li H, Xue J, Zhan M, Tang Q. Wall thickness variation of a superalloy thin-walled w-section seal ring during roll forming. J Netshape Form Eng 2019;11:43–9.

[6]    Yang L, Tao NR, Lu K, Lu L. Enhanced fatigue resistance of Cu with a gradient nanograined surface layer. Scr Mater 2013;68:801–4. https://doi.org/10.1016/J.SCRIPTAMAT.2013.01.031.

[7]    Guan Y, Chen B, Zou J, Britton T Ben, Jiang J, Dunne FPE. Crystal plasticity modelling and HR-DIC measurement of slip activation and strain localization in single and oligo-crystal Ni alloys under fatigue. Int J Plast 2017;88:70–88. https://doi.org/10.1016/J.IJPLAS.2016.10.001.

[8]    Dunne FPE, Wilkinson AJ, Allen R. Experimental and computational studies of low cycle fatigue crack nucleation in a polycrystal. Int J Plast 2007;23:273–95. https://doi.org/10.1016/J.IJPLAS.2006.07.001.

[9]    Bieler TR, Eisenlohr P, Roters F, Kumar D, Mason DE, Crimp MA, et al. The role of heterogeneous deformation on damage nucleation at grain boundaries in single phase metals. Int J Plast 2009;25:1655–83. https://doi.org/10.1016/J.IJPLAS.2008.09.002.

[10] Bracquart B, Mareau C, Saintier N, Morel F. Experimental study of the impact of geometrical defects on the high cycle fatigue behavior of polycrystalline aluminium with different grain sizes. Int J Fatigue 2018;109:17–25. https://doi.org/10.1016/j.ijfatigue.2017.12.009.

[11] Taylor DD. Sealing ring with e-shaped radial section 1965.

[12] Gao P, Yu C, Fu M, Xing L, Zhan M, Guo J. Formability enhancement in hot spinning of titanium alloy thin-walled tube via prediction and control of ductile fracture. Chinese J Aeronaut 2022;35:320–31. https://doi.org/10.1016/J.CJA.2021.01.002.

[13] Gao PF, Yan XG, Li FG, Zhan M, Ma F, Fu MW. Deformation mode and wall thickness variation in conventional spinning of metal sheets. Int J Mach Tools Manuf 2022;173:103846. https://doi.org/10.1016/J.IJMACHTOOLS.2021.103846.

[14] Li R, Zheng Z, Zhan M, Zhang H, Lei Y. A comparative study of three forms of an uncoupled damage model as fracture judgment for thin-walled metal sheets. Thin-Walled Struct 2021;169:108321. https://doi.org/10.1016/J.TWS.2021.108321.

[15] He Z, Zhang K, Zhu H, Lin Y, Fu MW, Yuan S. An anisotropic constitutive model for forming of aluminum tubes under both biaxial tension and pure shear stress states. Int J Plast 2022;152:103259. https://doi.org/10.1016/J.IJPLAS.2022.103259.

[16] Magrinho JP, Silva MB, Centeno G, Moedas F, Vallellano C, Martins PAF. On the determination of forming limits in thin-walled tubes. Int J Mech Sci 2019;155:381–91. https://doi.org/10.1016/J.IJMECSCI.2019.03.020.

[17] Zhang H, Zhan M, Zheng Z, Li R, Lyu W, Lei Y. A Systematic Study on the Effects of Process Parameters on Spinning of Thin-Walled Curved Surface Parts With 2195 Al-Li Alloy Tailor Welded Blanks Produced by FSW. Front Mater 2021;8. https://doi.org/10.3389/fmats.2021.809018.

[18] Bai H, Cao H, Li Y, Yang L. Failure Analysis and Optimized Verification of Metal W-sealing Ring of Aero-engine at High Temperature. Lubr Eng 2018;43:127–31. https://doi.org/10.3969/j.issn.0254-0150.2018.10.022.

[19] Shao G, Li H, Zhang X, Zhan M, Li Z, Liu Q. External-internal composite spinning technology for forming thin-walled Ω-sectioned ring of superalloy. J Mater Process Technol 2021;291:117004. https://doi.org/10.1016/J.JMATPROTEC.2020.117004.

[20] Jia X, Chen H, Li X, Wang Y, Wang L. A study on the sealing performance of metallic C-rings in reactor pressure vessel. Nucl Eng Des 2014;278:64–70. https://doi.org/10.1016/J.NUCENGDES.2014.07.006.

[21] Shen M, Peng X, Xie L, Meng X, Li X. Deformation Characteristics and Sealing Performance of Metallic O-rings for a Reactor Pressure Vessel. Nucl Eng Technol 2016;48:533–44. https://doi.org/10.1016/J.NET.2015.11.009.

[22] Wang X-Y, Zhu S-F, Wang X, Zhang X-C. Stress and thickness calculation of a bolted flat cover with double metal sealing rings. Nucl Sci Tech 2018;29:120. https://doi.org/10.1007/s41365-018-0457-2.

[23] Zhang M, Suo S, Feng Y, Shi J, Meng G. Parametric Analysis of Wave-shaped Metal Sealing Ring Based on Hierarchical Solution Method. IOP Conf Ser Mater Sci Eng 2019;616:012021. https://doi.org/10.1088/1757-899X/616/1/012021.

[24] Wang Y, Luo W, Liu S, Feng H, Li J, Wang J. A model for reliability assessment of sealing performance of the C-shaped metal sealing ring at the outlet of the subsea tubing hanger. Ocean Eng 2022;243:110311. https://doi.org/10.1016/J.OCEANENG.2021.110311.

[25] Hu G, Wang G, Dai L, Zhang P, Li M, Fu Y. Sealing Failure Analysis on V-Shaped Sealing Rings of an Inserted Sealing Tool Used for Multistage Fracturing Processes. Energies 2018;11. https://doi.org/10.3390/en11061432.

[26] Ding XY, Chen X. Analysis of Influence of Structures and Strength about Corrugated Radius of Metallic Sealing Ring. Adv Mater Res 2014;971–973:872–6. https://doi.org/10.4028/www.scientific.net/AMR.971-973.872.

[27] Zhang J, Hu Y. Mechanical behavior and sealing performance of metal sealing system in roller cone bits. J Mech Sci Technol 2019;33:2855–62. https://doi.org/10.1007/s12206-019-0533-5.

[28] Zheng Z, Balint DS, Dunne FPE. Rate sensitivity in discrete dislocation plasticity in hexagonal close-packed crystals. Acta Mater 2016;107:17–26. https://doi.org/10.1016/J.ACTAMAT.2016.01.035.

[29] Dunne FPE, Rugg D, Walker A. Lengthscale-dependent, elastically anisotropic, physically-based hcp crystal plasticity: Application to cold-dwell fatigue in Ti alloys. Int J Plast 2007;23:1061–83. https://doi.org/10.1016/J.IJPLAS.2006.10.013.

[30] Prastiti NG, Xu Y, Balint DS, Dunne FPE. Discrete dislocation, crystal plasticity and experimental studies of fatigue crack nucleation in single-crystal nickel. Int J Plast 2019;126:102615. https://doi.org/10.1016/J.IJPLAS.2019.10.003.

[31] Chen B, Jiang J, Dunne FPE. Microstructurally-sensitive fatigue crack nucleation in Ni-based single and oligo crystals. J Mech Phys Solids 2017;106:15–33. https://doi.org/10.1016/J.JMPS.2017.05.012.

[32] Chen B, Jiang J, Dunne FPE. Is stored energy density the primary meso-scale mechanistic driver for fatigue crack nucleation? Int J Plast 2018;101:213–29. https://doi.org/10.1016/J.IJPLAS.2017.11.005.

[33] Zhang T, Collins DM, Dunne FPE, Shollock BA. Crystal plasticity and high-resolution electron backscatter diffraction analysis of full-field polycrystal Ni superalloy strains and rotations under thermal loading. Acta Mater 2014;80:25–38. https://doi.org/10.1016/J.ACTAMAT.2014.07.036.

[34] Zhang T, Jiang J, Shollock BA, Britton T Ben, Dunne FPE. Slip localization and fatigue crack nucleation near a non-metallic inclusion in polycrystalline nickel-based superalloy. Mater Sci Eng A 2015;641:328–39. https://doi.org/10.1016/J.MSEA.2015.06.070.

[35] Swaminathan S, Ghosh S, Pagano NJ. Statistically Equivalent Representative Volume Elements for Unidirectional Composite Microstructures: Part I - Without Damage. J Compos Mater 2005;40:583–604. https://doi.org/10.1177/0021998305055273.

[36] Swaminathan S, Ghosh S. Statistically Equivalent Representative Volume Elements for Unidirectional Composite Microstructures: Part II - With Interfacial Debonding. J Compos Mater 2005;40:605–21. https://doi.org/10.1177/0021998305055274.

[37] Bagri A, Weber G, Stinville J-C, Lenthe W, Pollock T, Woodward C, et al. Microstructure and Property-Based Statistically Equivalent Representative Volume Elements for Polycrystalline Ni-Based Superalloys Containing Annealing Twins. Metall Mater Trans A 2018;49:5727–44. https://doi.org/10.1007/s11661-018-4858-y.

[38] Tu X, Shahba A, Shen J, Ghosh S. Microstructure and property based statistically equivalent RVEs for polycrystalline-polyphase aluminum alloys. Int J Plast 2019;115:268–92. https://doi.org/10.1016/J.IJPLAS.2018.12.002.

[39] Pinz M, Benzing JT, Pilchak A, Ghosh S. A microstructure-based porous crystal plasticity FE model for additively manufactured Ti-6Al-4V alloys. Int J Plast 2022;153:103254. https://doi.org/10.1016/J.IJPLAS.2022.103254.

[40] Wan VVC, MacLachlan DW, Dunne FPE. A stored energy criterion for fatigue crack nucleation in polycrystals. Int J Fatigue 2014;68:90–102. https://doi.org/10.1016/J.IJFATIGUE.2014.06.001.

[41] Kamlah M, Haupt P. On the Macroscopic Description of Stored Energy and Self Heating During Plastic Deformation. Int J Plast 1997;13:893–911. https://doi.org/10.1016/S0749-6419(97)00063-6.

[42] Wilson D, Zheng Z, Dunne FPE. A microstructure-sensitive driving force for crack growth. J Mech Phys Solids 2018;121:147–74. https://doi.org/10.1016/j.jmps.2018.07.005.

[43] Wilson D, Dunne FPE. A mechanistic modelling methodology for microstructure-sensitive fatigue crack growth. J Mech Phys Solids 2019;124:827–48. https://doi.org/10.1016/J.JMPS.2018.11.023.

[44] Wilson D, Wan W, Dunne FPE. Microstructurally-sensitive fatigue crack growth in HCP, BCC and FCC polycrystals. J Mech Phys Solids 2019;126:204–25. https://doi.org/10.1016/j.jmps.2019.02.012.

[45] Wan W, Dunne FPE. Microstructure-interacting short crack growth in blocky alpha Zircaloy-4. Int J Plast 2020:102711. https://doi.org/10.1016/J.IJPLAS.2020.102711.

[46] Zheng Z, Prastiti NG, Balint DS, Dunne FPE. The dislocation configurational energy density in discrete dislocation plasticity. J Mech Phys Solids 2019;129:39–60. https://doi.org/10.1016/J.JMPS.2019.04.015.

[47] He Y, Li Z. Personal communication 2021.

[48] Zheng Z, Li R, Zhan M, Yuan G, Zhang H, Lei Y, et al. The effect of strain rate asymmetry on the Bauschinger effect: A discrete dislocation plasticity analysis. J Mater Res Technol 2022;16:1904–18. https://doi.org/10.1016/J.JMRT.2021.12.107.